ACS PHYSICAL CHEMISTRY Au
AN OPEN ACCESS JOURNAL OF THE AMERICAN CHEMICAL SOCIETY

pubs.acs.org/physchemau

Article

Characterization of Nanoparticles in Diverse Mixtures Using Localized Surface Plasmon Resonance and Nanoparticle Tracking by Dark-Field Microscopy with Redox Magnetohydrodynamics Microfluidics

Jazlynn C. Sikes,[§] Kevin Wonner,[§] Aaron Nicholson, Paolo Cignoni, Ingrid Fritsch,* and Kristina Tschulik*

Cite This: *ACS Phys. Chem Au* 2022, 2, 289–298

Read Online

ACCESS | Metrics & More | Article Recommendations | Supporting Information

ABSTRACT: Redox magnetohydrodynamics (RMHD) microfluidics is coupled with dark-field microscopy (DFM) to offer high-throughput single-nanoparticle (NP) differentiation *in situ* and *operando* in a flowing mixture by localized surface plasmon resonance (LSPR) and tracking of NPs. The color of the scattered light allows visualization of the NPs below the diffraction limit. Their Brownian motion in 1-D superimposed on and perpendicular to the RMHD trajectory yields their diffusion coefficients. LSPR and diffusion coefficients provide two orthogonal modalities for characterization where each depends on a particle's material composition, shape, size, and interactions with the surrounding medium. RMHD coupled with DFM was demonstrated on a mixture of 82 ± 9 nm silver and 140 ± 10 nm gold-coated silica nanospheres. The two populations of NPs in the mixture were identified by blue/green and orange/red LSPR and their scattering intensity, respectively, and their sizes were further evaluated based on their diffusion coefficients. RMHD microfluidics facilitates high-throughput analysis by moving the sample solution across the wide field of view absent of physical vibrations within the experimental cell. The well-controlled pumping allows for a continuous, reversible, and uniform flow for precise and simultaneous NP tracking of the Brownian motion. Additionally, the amounts of nanomaterials required for the analysis are minimized due to the elimination of an inlet and outlet. Several hundred individual NPs were differentiated from each other in the mixture flowing in forward and reverse directions. The ability to immediately reverse the flow direction also facilitates re-analysis of the NPs, enabling more precise sizing.

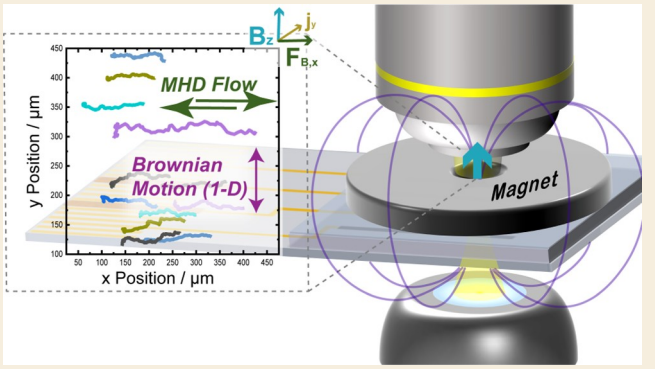

KEYWORDS: *redox magnetohydrodynamics, dark-field microscopy, nanoparticles, microfluidics*

1. INTRODUCTION

The rising interest in commercial and industrial use of nanoparticles (NPs) and nanomaterials has greatly outpaced the fundamental understanding of their properties. Applications for nanomaterials range from catalysts for alternative energy technologies and processes (*e.g.*, fuel cells, photochemical energy conversion, and reactions involving hydrocarbons[1−5]) to antimicrobials in medical devices.[6,7] Their physical properties differ from their bulk phase counterparts, for example, due to the higher surface energy of the NPs.[2,8−10] The characteristics are not only affected by variation in composition but also strongly dependent on the particle size and shape.[9,11−13] There exists a knowledge gap with respect to the properties and chemical reactivities of nanomaterials.[14−16] Methods to evaluate NPs in a solution are limited, and because NPs are heterogeneously sized and shaped, statistically relevant populations must be investigated. This is especially challenging for dilute samples where larger volumes need to be evaluated to attain statistical relevance. Yet, it is also essential to be able to study the individualized behavior of each NP within that population to determine how it contributes toward the collective behavior. The increasing use of different nanomaterials containing unknown environmental risks[17−20] in everyday products and industrial applications is creating an urgent demand for analyzing NPs in mixtures in a reliable, easy, and rapid manner. Thus, having tools that allow for high-

Received: December 1, 2021
Revised: January 6, 2022
Accepted: January 11, 2022
Published: January 25, 2022

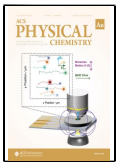

throughput single-entity evaluation in solution environments is paramount. Here, microfluidics driven by redox magnetohydrodynamics (RMHD), which provides highly controlled sample delivery across a wide viewing window, is coupled with dark-field microscopy (DFM) for tracking, analyzing, and identifying NPs to address this need. RMHD also minimizes the NP waste, and therefore cost, because the inlets, outlets, and reservoirs of fluid are not required. Hence, NP solutions of a few microliters can be analyzed.

There are various increasingly common methods used for characterizing the NP size and shape distribution. Transmission electron microscopy (TEM) and scanning electron microscopy (SEM) can achieve high spatial resolution and imaging of the morphological features of individual NPs, respectively, but are generally performed *in vacuo*. Recently, TEM has been interfaced with a liquid cell, but applications are limited to liquids with low vapor pressure and still require the complexity and maintenance of operating a vacuum system.[21] Dynamic light scattering (DLS) is performed *in situ* and allows real-time monitoring of changes to hydrodynamic radius occurring in suspension but for an average of the population. The presence of just a few larger particles can drastically skew the calculated size[22] because intensity scaling depends on the volume of the particles squared, leading to an inaccurate quantification of the distribution. Scattered light can be used to visualize and follow individual NPs in suspension with NP tracking analysis (NTA). This technique differentiates between particles from differences in their Brownian motion (and therefore diffusion coefficients). NTA can be coupled with fluid flow from a syringe pump to increase the throughput. Single-laser NTA, such as DLS, however, suffers from inaccurate determination of size distributions in polydisperse samples because only the intensity of scattered light, which is a strong function of size, is tracked.[23] NTA using multiple lasers of different wavelengths resolves this problem, but a flowing sample is not an option, and this technique comes with a high price tag.[24,25] DFM, however, which is used here, has the advantage that it can monitor and differentiate individual NPs *in situ* and *operando* in a relatively inexpensive way and can be coupled with a flowing sample and other analytical techniques. This allows physical and chemical information to be obtained from the NPs.[26−29] The ability of DFM to image NPs exhibiting localized surface plasmon resonance (LSPR) is especially notable because LSPR scatters specific wavelengths more strongly and results in a higher sensitivity to a particle's properties than the case for laser-based techniques.[30,31] Scattered light is observed through an objective lens, which allows visualization of NPs below the diffraction limit when illuminated by a white light source. This is not achievable with other conventional forms of microscopy (*e.g.*, bright field and fluorescence) where distinguishing between the absorbed light and the re-emitted light of the same wavelength in the same radiation path is impossible. Furthermore, the spectral signature of the scattered radiation, which is indicative of size, shape, and composition, from each NP can be measured.

LSPR, first described by Faraday in 1857,[32] is based on the interaction of light with nanostructures and determines the color of plasmonic NP suspensions. Because only non-transmitted light is detected in DFM, it is useful for observing individual NPs that exhibit strong LSPRs such as silver, gold, and copper,[33−36] as well as for monitoring their chemical reactions and events at their surfaces.[37−41] DFM combined with NP tracking analysis has been previously used to determine their diffusion coefficients by tracing the random paths of NPs in a static suspension.[33] In addition to providing diffusion coefficients, single-particle tracking facilitates detailed observation of how a NP interacts with its surrounding environment. Methods have been developed with this approach to monitor the behavior of particles in suspension[42−44] and the uptake of particles into bacteria.[45]

A flowing sample of NPs is of interest for analyzing more particles than in a static solution. However, to observe diffusion of NPs, uncontrolled sources of fluid movement and vibrations must be either prevented or managed. In classical mechanical pumping, which is commonly used for NP tracking methods, the pressure gradient results in a parabolic flow profile with an intermittent pulsatile behavior and vibrations.[46] This can complicate deconvolution of the superimposed Brownian motion. Larger volumes of NP samples are also needed than the actual volume analyzed because of the extra volume required for the reservoir and tubing. Additionally, diffusion coefficient analysis is limited to a single examination of a given suspension volume because reversible pumping and tracking are not manageable. Electroosmotic pumping generally results in a flat flow profile[47] but depends on the physicochemical properties of the walls of a very narrow channel (10−100 μm in width and height) that guides the fluid. Additionally, charged NPs will migrate in the applied electric field. To overcome these constraints, we have coupled RMHD with DFM (RMHD−DFM) to provide a method of highly controlled fluid movement, facilitating differentiation of NPs by both LSPR and diffusion coefficient in a flowing suspension. RMHD−DFM provides the ability to observe particles over a wide field with a reversible and uniform flow profile in a given horizontal plane[48] and without high electric fields. The total sample volume can also be limited to that of the analysis chamber.

RMHD microfluidics is propelled by the magnetic portion of the Lorentz force, the magnetohydrodynamic force $\mathbf{F}_B$, following the right-hand rule (eq 1)[48−52]

$$\mathbf{F}_B = \mathbf{j} \times \mathbf{B} \tag{1}$$

where $\mathbf{j}$ is the ionic current density and $\mathbf{B}$ is the magnetic flux density. This relationship gives RMHD its unique ability to program microfluidics—to stop, start, reverse, and tune flow without requiring valves or retooling a device. A sample solution is added to a chip patterned with individually addressable electrodes and placed adjacent to a permanent magnet. When an electronic current is passed between electrodes which have been modified with the conducting polymer poly(3,4-ethylenedioxythiophene) (PEDOT), the polymer oxidizes at the anode, attracting anions from the electrolyte solution to compensate charge (and repels cations) and the opposite process occurs at the cathode, thus creating the ionic current.[48,53] The uniform horizontal flow profile of RMHD has enabled imaging of leukocytes of 10s μm in a flowing sample with fluorescence epitaxial light sheet confocal microscopy.[50] RMHD has also been combined with fluorescence correlation spectroscopy[54] to attain flow profiles and diffusion coefficients of particles down to 0.1 μm but without direct imaging capabilities.

Here, PEDOT-modified RMHD microfluidics is used for samples with the smallest particles pumped by this approach to date and provides the precise control needed to enable flow DFM for NP analysis. Flow DFM is used to identify, quantify, and size a flowing suspension mixture of two types of NPs,

https://doi.org/10.1021/acsphyschemau.1c00046
ACS Phys. Chem Au 2022, 2, 289−298

silver and silica core gold shell (Ag and SiO_2@Au), in a volume beyond the confines of the microscope's viewing window. Silver[41,55] and silica core gold shell[56,57] were chosen because they are widely studied materials and are frequently used NPs for investigation with DFM and thus serve as excellent model systems for coupled RMHD−DFM.[31] The NP types are detected and differentiated from each other based on the scattered light with blue/green and orange/red wavelengths from their LSPR, respectively, which also allows visualization of the small nanoscopic entities.[33] Detecting the intensity and wavelength of scattered light gives insight into the size, shape, composition, and chemical environment within one sample and additionally allows determination of diffusion coefficients by tracking those NPs in the moving suspension. Furthermore, the pumping direction is reversed to provide multiple observations of the same subvolumes of the sample. This allows more precise information about the size distribution to be obtained compared to a unidirectional pumping system. Additionally, the ability to reverse pumping increases the probability of observing NPs previously outside of the plane of view, permitting the analysis of samples with low NP concentrations.

2. EXPERIMENTAL SECTION

Details about the chemicals and materials and their sources are provided in the Supporting Information.

2.1. Preparation of PEDOT-Modified Chip Electrodes

Gold band electrodes with a chromium adhesion layer (nominally, 650 μm wide, 1.5 cm long, and 0.25 μm thick) were patterned onto a borosilicate glass wafer *via* conventional photolithography similar to that previously described for silicon wafers.[58] The patterned wafer was then diced into 2.54 cm × 5.08 cm (1 in × 2 in) chips. The separation of the inner pair of electrodes, which were activated for RMHD pumping, measures 0.47 cm. The outermost band electrodes and other smaller electrodes on the chip were not used in the studies reported here.

A film of PEDOT was sequentially electropolymerized onto each band electrode based on a previously described procedure[53] (modifications to the referenced procedure are in the Supporting Information) and used as a working electrode (WE). Cyclic voltammetry (CV) was performed with a PalmSens4 galvanostat/potentiostat (Palmsens, Houten, the Netherlands), a platinum counter electrode (CE), and a Ag/AgCl, 3 M KCl reference electrode (RE). The chip was then rinsed with propylene carbonate and water and stored in water until use. A photo of the chip with PEDOT-deposited electrodes (Figure S1) and additional details of electropolymerization can be found in the Supporting Information.

2.2. RMHD Flow DFM Experimental Setup

Optical tracking of the NPs with RMHD−DFM was achieved by the assembly depicted in Figure 1a. DFM was performed using an Olympus BX43 Microscope, equipped with a 10× Plan Achromat Objective, a CytoVita Optical Illuminator, which includes a halogen lamp and a liquid light guide, and a Retiga R1 OEM CCD camera operated at 9.9 fps. Non-scattered light is blocked by apertures, while light specifically scattered by the sample reaches the objective. Hence, only light which interacts with the sample is focused and detected, and all else appears black, specifically, allowing the detection of nanosized plasmon-active structures by their LSPR.

The RMHD apparatus, shown in Figure 1b, containing the suspension of NPs was placed in a 3D-printed polylactic acid holder onto the movable stage of the DFM microscope. This apparatus consisted of a special transparent electrochemical cell coupled with the NdFeB permanent ring magnet, **B**, and connected to the galvanostat/potentiostat to allow activation of the pumping electrodes by producing an ionic current, **j**, thereby engaging RMHD microfluidics. A 700 μm-thick poly(dimethylsiloxane) film, into

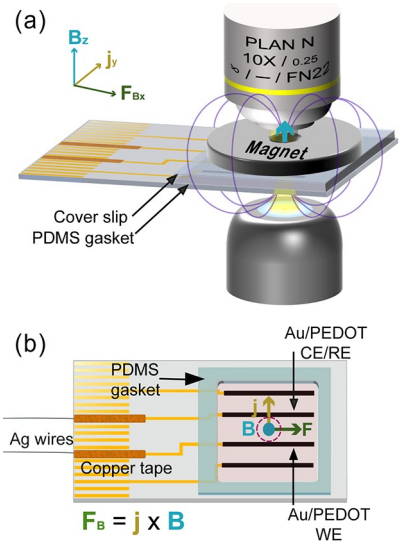

Figure 1. RMHD−DFM setup. (a) Electrochemical cell/magnet assembly used for RMHD−DFM is located between the illuminating system and the microscope objective. The coordinate system assignments and the directions are also shown for the applied **j**, **B** from the magnet, and $\mathbf{F}_B$, which directs fluid flow between the activated electrodes. (b) Top-down view of the electrochemical portion of the RMHD assembly showing the innermost band electrodes that are activated. The region inside the poly(dimethylsiloxane) gasket contains the NP suspension. The DFM viewing field of the microscope is indicated by the dashed circle.

which a rectangular opening large enough to accommodate all the four large band electrodes was cut, was first placed on the chip, then 400 μL of NP suspension was pipetted into it, and topped with a coverslip. Excess NP suspension was carefully blotted with a Kimwipe. Connections to the potentiostat/galvanostat were made through silver wires that were adhered to the chip's contact pads with conductive copper tape. No external reservoir was used, and only the pipetted NP suspension was pumped within the cell.

The ring magnet with an outer diameter of 24.8 mm and a thickness of 2.5 mm, containing a 5 mm diameter hole (Figure S2 of the Supporting Information), was placed atop the coverslip. The hole in the center of the magnet is necessary for the transmission of light. The outer dimensions of the magnet were chosen to be as large as possible to maximize the magnetic flux, but when combined with the electrochemical chamber, they would be small enough for the assembly to fit on the stage between the objective lens and the light source. The magnetic flux measured 270 mT where the center of the hole contacted the coverslip.

2.3. Operation and Characterization for RMHD−DFM

Three different NP suspensions in 50 mM KNO_3 were evaluated by DFM. One contained 137 nm SiO_2@AuNP, another contained 70 nm AgNP, and the other was prepared as a mixture of 70 nm AgNP and 137 nm SiO_2@AuNP (These diameters are those reported by the manufacturer). The separate suspensions of AgNPs and SiO_2@AuNPs were used to confirm the color associated with the type of the particle and to confirm that the NPs would not agglomerate significantly in the 50 mM KNO_3 electrolyte during the studies. An image of the SiO_2@AuNPs under dark-field illumination is depicted in Figure S3 of the Supporting Information. All suspensions were sonicated with an Emmi-12 HC from EMAG AG for *ca.* 7 s at 100% intensity before use.

For RMHD pumping studies, one PEDOT-modified gold electrode was used as the WE, and another was used as a combined CE/RE. Due to small current and small distances between WE and CE/RE and a resulting negligible Ohmic drop, a two-electrode setup can be used (Figure 1b). Chronopotentiometry (CP) was performed with

https://doi.org/10.1021/acsphyschemau.1c00046
ACS Phys. Chem Au 2022, 2, 289−298

three sequential 15 s current steps, without breaks, starting at +50 μA (forward 1), switching to −50 μA (reverse), and then repeating +50 μA (forward 2). This sequence was carried out both in the presence and in the absence of the magnet, which can be seen in Videos S1 and S2 in the Supporting Information, respectively. The latter served as a control experiment to determine the underlying motion that is independent of RMHD microfluidics.

2.4. Characterization of NPs by Electron Microscopy and Dynamic Light Scattering

Scanning transmission electron microscopy (STEM) images of NPs were recorded on a JEOL JEM-2800 electron microscope equipped with a Schottky electron gun working at 200 kV. The point-to-point resolution is 0.14 nm. Elemental mapping by energy-dispersive X-ray (EDX) spectroscopy was obtained with JEOL double-SDD X-ray detectors, with a 133 eV spectral resolution, a solid angle of 0.98 sr, and a detection area of 100 mm^2. Each sample was prepared by drop-coating the NP suspensions on a PLANO S-160 TEM grid (carbon film on 200 mesh copper grid). DLS was performed with a Zetasizer Ultra (Malvern Panalytical GmbH). The NP suspensions were measured with a HeNe Laser of 633 nm.

2.5. Color Processing of LSPR Images to Identify the NP Type

To determine the color assignments, a pure suspension of SiO_2@AuNPs in 50 mM KNO_3 was analyzed using ImageJ.[59] Figure S3 depicts the range of their red/orange LSPR colors. Using the color threshold tool in ImageJ, the red/orange group, hues 0−55, was assigned to SiO_2@AuNPs and the blue/green group, hues 56−255, was assigned to AgNPs. The video for the mixed NP suspension was then converted to individual frames, imported as an image sequence, and filtered to produce two sets of images by adjusting the color threshold. Black was chosen to replace all "filtered" colors. After color separation, the MosaicSuite plugin[60] for ImageJ was used to track the particles and provide the (x, y) coordinates of each particle track.

3. RESULTS

3.1. RMHD−DFM of AgNPs and SiO_2@AuNPs and Comparison to TEM Results

The STEM images and EDX mappings of the AgNPs and SiO_2@AuNPs shown in Figure 2 confirm the shape, size, and

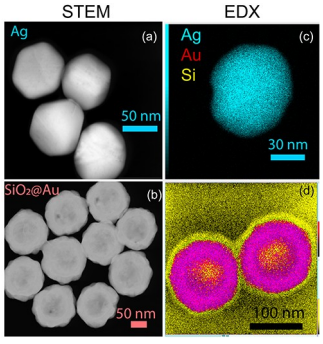

Figure 2. STEM and EDX spectroscopy images of 82 ± 9 nm AgNPs in (a,c) and 140 ± 10 nm SiO_2@AuNPs in (b,d).

composition of the NPs. The shapes are spherical, and the averaged diameters were calculated by an arithmetic mean measure of 82 ± 9 nm and 140 ± 10 nm, respectively. The standard deviation around the average measured diameter for the SiO_2@AuNPs brackets the manufacturer's reported diameter of 137 nm. However, the TEM-measured diameter for the AgNPs is larger than the manufacturer's 70 nm specification. The color based on LSPR appears blue/green for the AgNPs and red/orange for the SiO_2@AuNPs. Figure 3 is a

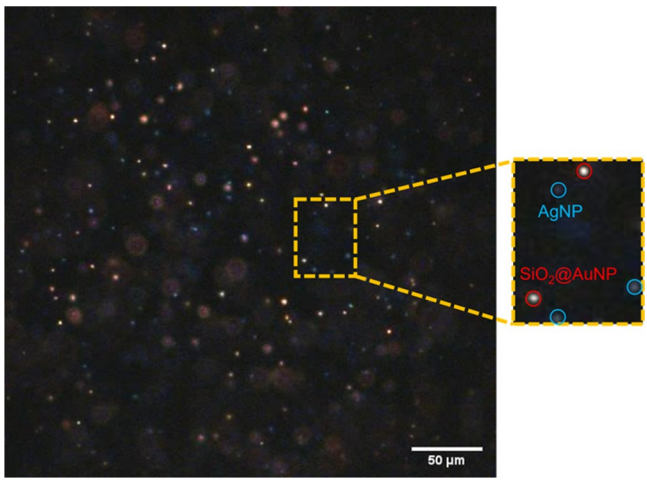

Figure 3. DFM image of the mixed AgNP and SiO_2@AuNP suspension in 50 mM KNO_3 with an exposure time of 100 ms and a magnification of 10×. The image is taken from a video recorded during the application of +50 μA current and in the absence of the magnet (non-pumped). The NPs containing a "halo" were deemed to be too much out-of-focus for tracking purposes, and only NPs without a "halo" were tracked. The orange box indicates an enhanced zoom and shows representative AgNPs and SiO_2@AuNPs in blue and red, respectively.

snapshot taken by DFM of the mixture in the RMHD apparatus. The count of particles belonging to the two different populations based on the color differentiation yields a measured ratio of AgNPs to SiO_2@AuNPs in the suspension of 58 ± 5 to 42 ± 6%, respectively.

3.2. Effect of RMHD on NP Motion

The tracks of the individual movements of the particles shown in Figure 3 are given in Figure 4a for the case where a current is applied in the absence of the magnet, showing only a non-directed behavior. However, in the presence of the magnet, RMHD induces a net displacement along the x-direction, as expected. Figure 4b displays the resulting particle tracks involving both Brownian motion and the RMHD trajectory. The contribution of diffusion is easily observable in the y-direction, perpendicular to the RMHD flow. The displacements are small, however, compared to the RMHD travel distance. Note that only the particles moving in the z-direction that remained in focus long enough to provide a sufficient tracking length in the $x-y$ plane were considered for particle analysis to ensure appropriate sizing.

Video S1 of the Supporting Information is a recording of the mixture of NPs obtained by DFM in the presence of the magnet from which Figure 4b was obtained. It shows the apparent random NP movement when the pumping electrodes are off at the beginning of the video. A net translation in the $+x$-direction is superimposed on the random movement when a current of +50 μA is applied between the electrodes (examples of particle displacements are depicted in Figure S4 of the Supporting Information), a quick change of translation in the $-x$-direction occurs when the current is switched to −50 μA, and a reversal of direction again in the $+x$-direction happens when the current returns to +50 μA. The waveform of the applied current over time, a representative plot of the recorded potential, and the corresponding analysis are provided in Figure S5 in the Supporting Information. When the current returns to zero after 45 s, translation in the x-

https://doi.org/10.1021/acsphyschemau.1c00046
ACS Phys. Chem Au 2022, 2, 289−298

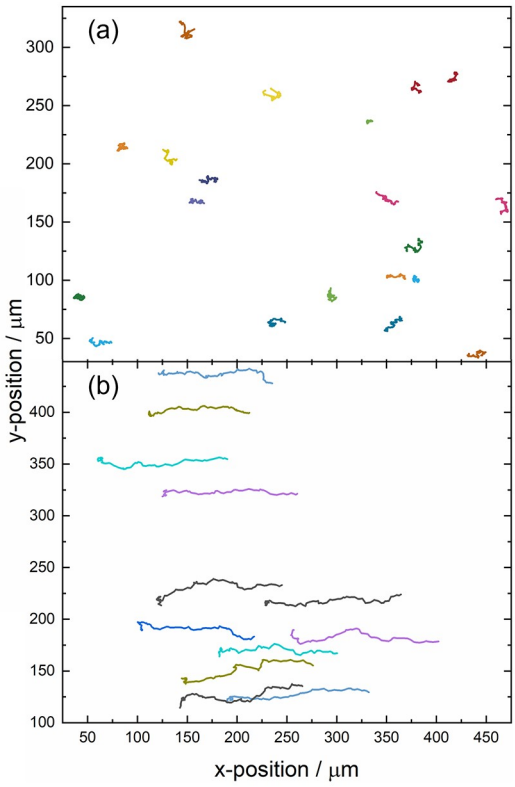

Figure 4. NP tracks of the mixed NP suspension in 50 mM KNO_3 over 74 frames (7.4 s) during an applied current of +50 μA and in the (a) absence and (b) presence of the magnet (flow direction to positive *x*-positions).

direction ends and random movement remains. RMHD creates a reversible vibration-free "pump" within the cell volume by switching the polarity of the electrodes to reverse the direction of the fluid movement, so long as the magnet orientation remains unchanged.

Video S2 of the Supporting Information is a recording of an experimental sequence like that in Video S1, but in the absence of a magnetic field, and from which Figure 4a was obtained. The NPs remain dominated by Brownian motion in the presence of an applied current, regardless of its direction. A plot comparing the displacements for multiple NPs for each part of this experiment is shown in Figure S6 of the Supporting Information. A slight negative charge on the NPs might subject them to electrophoresis toward the anode. However, there is no discernible net translation toward the anode or the cathode, indicating that migration for individual NPs in the electric field is insignificant. A more detailed discussion of the direction and speed of NP motion with and without RMHD pumping is provided in the Supporting Information.

To observe the Brownian motion of NPs in a moving suspension, the fluid velocity must be slow enough for several random steps to be visible while the NPs remain in the field of view. The average speed of the RMHD flow under our conditions was measured to be 13.9 ± 1.5 μm s^{-1} for the blue/green NPs and 13.7 ± 1.4 μm s^{-1} for the red/orange NPs. The speed information for each forward and reverse excursion can be found in Table S1 of the Supporting Information. The pumping speeds were determined by dividing the distance between the first and last point of the particle tracks by the time between those positions. The velocity within individual NP tracks varied significantly due to the contribution from the particles' random motion, which is most noticeable by sideways deviations from a line connecting the starting and ending positions. Because the Brownian motion along the RMHD-driven translation is expected to be random (equal displacements in forward and reverse directions), it should only affect the measurement of the RMHD fluid speed in the form of the standard deviation around the average.

3.3. Determination of NP Sizes from Diffusion Coefficients in the Absence of RMHD Flow

The diffusion coefficients, which were used to calculated the size of the NPs assuming a spherical shape, of the different populations of AgNPs and SiO_2@AuNPs in the mixture were determined first in the absence of RMHD flow, without the magnet and with the current engaged, setting a baseline for obtaining information and providing insight into whether migration is of significance.

Mean-square displacement (MSD) plots, which have been previously used for the sizing of individual particles,[33,39,61−67] were generated for each particle track. MSD plots were produced from the movement of NPs having a minimum of 30 steps in their tracks. The average MSD value in the *y*-direction for each time step (τ) 1−5 over the entire track length was calculated in cm^2 s^{-1}, and τ was converted to seconds. From these plots, the diffusion coefficients D for each NP can be extracted from the slope of the least-squares regression, and then the hydrodynamic radius can be estimated using the Stokes−Einstein equation[68] (eq 2), where k_B is the Boltzmann constant, T is the temperature, μ is the viscosity, and r is the hydrodynamic radius of the particle.

$$D = \frac{k_B \times T}{6\pi \times \mu \times r} \tag{2}$$

Any lines with an R^2 (coefficient of determination) of <0.8 were not included in the calculation for an average NP size.

The NPs were additionally analyzed with NanoTrackJ,[33] a method in which the diffusion of particles is tracked, and the results are depicted in Figure S7. The size distributions (Walker's method[69]) were centered at 105 and 135 nm for the blue/green and red/orange groups, respectively. Settings are listed in Table S2 in the Supporting Information. The total number of NPs tracked in the mixture was 733. The blue/green group contained 384 particles and the red/orange group contained 389 particles, indicating that the color analysis built into ImageJ was sufficient for the microscope and camera settings required for pairing with the magnet, though only a low-magnification objective was used.

Using our one-dimensional (1-D) MSD method, 417 blue/green and 360 red/orange particles were tracked. The particle sizes calculated from the position of the histogram peak maximum values were 86 ± 19 and 128 ± 32 nm for the blue/green and red/orange groups, respectively. Our 1-D MSD method agrees with the TEM-determined average size of 82 ± 9 nm for the AgNPs but slightly underestimates the TEM-determined average size of 140 ± 10 nm for the SiO_2@AuNPs. The similarity of the sizes determined by MSD under an applied current and TEM provides further support that migration is not playing a significant role in the mass transport of the NPs. Table S3 in the Supporting Information lists the NP sizes for both populations. DLS determined sizes (by the peak maxima of the obtained histograms) of 71 ± 1 nm for the AgNPs and 127 ± 1 nm for the SiO_2@AuNPs from pure

https://doi.org/10.1021/acsphyschemau.1c00046
ACS Phys. Chem Au 2022, 2, 289−298

suspensions. (DLS cannot provide such information from mixtures.)

3.4. Determination of NP Sizes from Diffusion Coefficients in the Presence of RMHD Flow

Analysis of the particle sizes during RMHD flow was carried out using the same method as previously described for the case without flow. Because the movement in the *x*-direction was assumed to be dominated by RMHD, only the *y*-dimension was used to create the plots of MSD *versus* time step (depicted in Figure S8 of the Supporting Information). This approach also has the advantage that the large displacement in *x* arising from the fluid flow more than offsets the low resolution and facilitates the measurement by a more easily discernible localization of the Δy displacement due to the Brownian motion, leading to a more precise measurement of the diffusion coefficients (Figure 4(b)). 1-D MSD curves were created from displacement along the *y*-axis with the average value for each $\tau = 1-5$ over the entire particle track (Figure S8). As in the case without RMHD flow, the diffusion coefficients were extracted from the slope, and the Stokes–Einstein equation (eq 2) was used to estimate the NP sizes. For each color associated with the NPs, the three pumping excursions (forward 1, reverse, and forward 2 segments of the video) were analyzed separately. The diffusion coefficients obtained in the pumped mixture (AgNPs and SiO_2@AuNPs) are summarized in a histogram in the Supporting Information in Figure S9. The size distributions, calculated from the diffusion coefficients and assuming spherically shaped NPs, are shown in Figures 5 and S10 (see the Supporting Information) for the AgNPs and the SiO_2@AuNPs, respectively. Particle diameters calculated to be smaller than 0 nm and larger than 500 nm were filtered out from the histograms. The data are summarized in Tables S3 and S4 in the Supporting Information, alongside the results obtained in the absence of RMHD flow.

As depicted in Figure 5, the blue/green group shows a maximum of the histograms around 72.5 and 107.5 nm for the pumped suspension and 82.5 nm for the non-pumped suspension with the magnet in place. Figure S10, indicating the size distribution of SiO_2@Au, shows that the red/orange groups were around 92.5 and 152.5 nm, respectively, for the pumped suspensions and 137.5 nm for the non-pumped suspension.

Figure 6 summarizes and compares the sizes of the two populations of NPs obtained by visualization with LSPR and subsequent 1-D MSD analysis for both static and RMHD-pumped mixtures (see Supporting Information Table S3) to the sizes obtained by TEM and DLS on pure suspensions. The results from 1-D MSDs for pumped and non-pumped suspensions show nearly the same average sizes for the AgNPs. The results for the single populations of AgNPs analyzed by TEM and DLS show comparable sizes, validating the method of using 1-D MSD plots to size nanomaterials in a pumped mixed suspension. For SiO_2@AuNPs, however, static non-pumped solutions show slightly higher average particle sizes compared to the pumped NP suspension and the results by TEM and DLS. In general, the herein presented method can distinguish NPs based on LSPR color (in our case, two different populations of different compositions) *in situ* and, in particular, *operando*, with subsequent analysis of diffusion coefficients, and thus size distributions, in the presence and absence of fluid dynamics, leading to a greater control of statistics and a possible implementation for microfluidic devices.

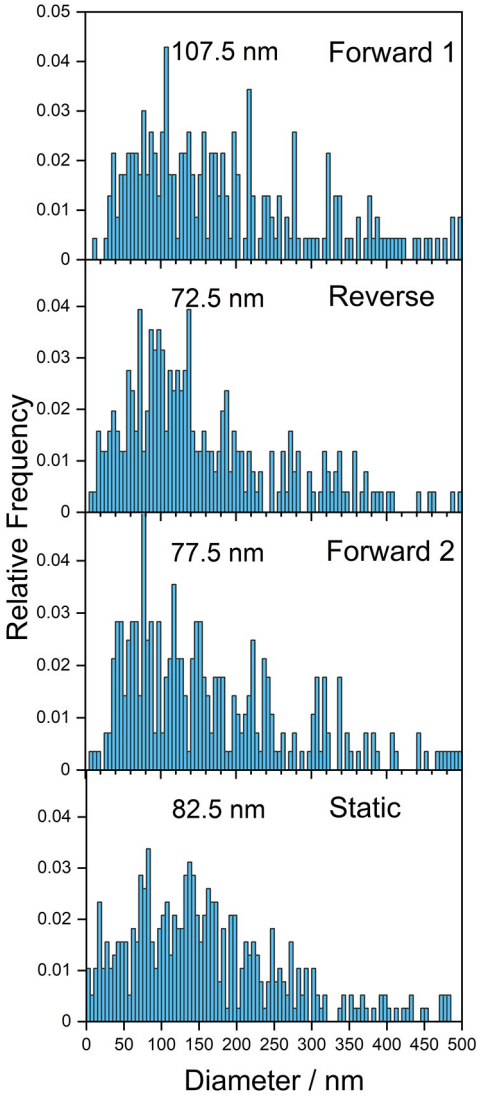

Figure 5. Size distributions of the NPs with LSPR having hues 56–255 assigned to AgNPs in the mixture and calculated from the 1-D MSD of the RMHD-pumped (forward 1, reverse, and forward 2) and of the non-pumped (static) suspension.

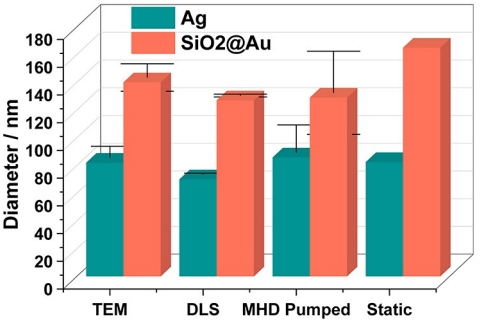

Figure 6. Comparison of size determination from several methods. The mixed suspension in 50 mM KNO_3 was used for the non-pumped (static) and RMHD-pumped method, and pure NP suspensions in the absence of KNO_3 were used for DLS and TEM. AgNPs are shown by teal bars, and SiO_2@AuNPs are shown by orange bars; the error bars represent the ±1 standard deviation.

https://doi.org/10.1021/acsphyschemau.1c00046
ACS Phys. Chem Au 2022, 2, 289–298

4. CONCLUSION

We have presented a method for combining DFM with self-contained RMHD microfluidics to facilitate single-particle analysis in mixtures of disperse NP populations, within the small sample volumes and without the disadvantages posed by other pumping methods such as vibrations. The adaptations made to previously reported RMHD configurations allow precisely controlled fluid motion into and out of the DFM field of view, leading to an increase in NP sampling capabilities and an assessment of NP movement. It can be concluded that RMHD−DFM can be used to efficiently characterize individuals and populations of NPs *in situ* and *operando* through two modalities, LSPR and diffusion coefficients, each with different dependencies on composition, shape, size, and interactions of the surrounding medium. Additionally, we have successfully demonstrated a new approach that determines diffusion coefficients of individual NPs in a mixture while they are in motion by calculating their respective 1-D MSDs.

We envision that RMHD−DFM can be applied to investigations of a broad range of NP suspensions, both aqueous and nonaqueous, for studies of dynamic interactions, catalysis, and synthesis. Here, we demonstrate the usage of RMHD−DFM as an efficient tool to both evaluate the NP sizes and simultaneously differentiate between mixtures of different nanomaterials. In addition, the presence of a magnetic field gradient can offer an extra factor of influence on the mass transport,[70−72] separation,[73,74] and interactions of (super)-paramagnetic NPs.[75] In addition, this method is well suited for probing samples with low NP concentrations. Moreover, even non-plasmonic particles can be visualized, although their scattering intensity is lower compared to plasmonic particles. The possibility for RMHD−DFM to achieve *operando* insights into the dynamic processes of nanomaterials may provide unique opportunities in process monitoring and control. In particular, agglomeration dynamics of NPs as a function of time could easily be detected as a change in color and diffusion coefficient with a change of the size of the grouped NPs by the present RMHD−DFM approach. Moreover, the prospects to simultaneously probe individual reactivity of different NPs in suspensions during chemical or electrochemical reactions and under constant flow may open new routes to study heterogeneous catalysis and control NP synthesis, growth, and dissolution.

■ ASSOCIATED CONTENT

Supporting Information

The Supporting Information is available free of charge at https://pubs.acs.org/doi/10.1021/acsphyschemau.1c00046.

Discussion of the chemicals and materials, electrode preparation, NP motion with and without RMHD pumping, and NanoTrackJ settings; pumping speeds for individual video sections; average NP diameter, mode diameter of the histograms, and median diameter calculated from 1-D MSD of each video segment; calculated AgNP and SiO_2@AuNP suspension percent ratio; chip used for RMHD−DFM; magnet used for RMHD; DFM image of SiO_2@AuNP in KNO_3; tracked NPs in DFM images; applied current waveform and response of potential; NP displacements with and without current in the absence of magnetic field; size distribution of AgNPs and SiO_2@AuNPs in the absence of a magnetic field and the presence of ionic current analyzed by NanoTrackJ; 1-D MSD plots of NP mixture; diffusion coefficient distributions of AgNPs and SiO_2@AuNPs calculated from 1-D MSD; size distributions of SiO_2@AuNPs calculated from 1-D MSD; and DFM images obtained during pumping (PDF)

Sequence of RMHD pumping carried out in the presence of a magnetic field (AVI)

Sequence of RMHD pumping carried out in the absence of a magnetic field (AVI)

■ AUTHOR INFORMATION

Corresponding Authors

Ingrid Fritsch − *University of Arkansas Department of Chemistry and Biochemistry, Fayetteville, Arkansas 72701, United States;* orcid.org/0000-0003-2900-5449; Email: ifritsch@uark.edu

Kristina Tschulik − *Ruhr University Bochum, Faculty of Chemistry and Biochemistry, Chair of Analytical Chemistry II, Bochum 44801, Germany;* orcid.org/0000-0001-7637-4082; Email: kristina.tschulik@rub.de

Authors

Jazlynn C. Sikes − *University of Arkansas Department of Chemistry and Biochemistry, Fayetteville, Arkansas 72701, United States;* orcid.org/0000-0002-2729-2328

Kevin Wonner − *Ruhr University Bochum, Faculty of Chemistry and Biochemistry, Chair of Analytical Chemistry II, Bochum 44801, Germany;* orcid.org/0000-0002-5300-4836

Aaron Nicholson − *University of Arkansas Department of Chemistry and Biochemistry, Fayetteville, Arkansas 72701, United States;* orcid.org/0000-0001-8139-1856

Paolo Cignoni − *Ruhr University Bochum, Faculty of Chemistry and Biochemistry, Chair of Analytical Chemistry II, Bochum 44801, Germany;* orcid.org/0000-0002-2457-9446

Complete contact information is available at: https://pubs.acs.org/10.1021/acsphyschemau.1c00046

Author Contributions

[§]These authors contributed equally.

Funding

J.S. acknowledges the Sturgis International Fellowship, a grant made possible by the generous support of the Roy and Christine Sturgis Charitable Trust. K.W. acknowledges a Ph.D. scholarship donated by the German Chemical Industry Fund (FCI Kekule Stipendium). This work was supported by the Research Training group "Confinement-controlled Chemistry", funded by the Deutsche Forschungsgemeinschaft (DFG) under grant GRK2376/331085229. This research was also funded by the National Science Foundation (CMI-1808286) and the Arkansas Biosciences Institute, a major research component of the Arkansas Tobacco Settlement Proceeds Act of 2000. We further acknowledge the funding by the Deutsche Forschungsgemeinschaft under Germany's Excellence Strategy—EXC 2033—390677874—RESOLV and the European Research Council (ERC) under the European Union's Horizon 2020 research and innovation programme (MITICAT; grant agreement no. 949724). K.T. acknowledges financial support from the Max Planck Fellowship Programme.

P.C. acknowledges the International Max Planck Research School SurMat for a doctoral scholarship.

Notes

The authors declare the following competing financial interest(s): I.F. declares a potential conflict of interest as she is listed as an inventor on a patent filed by the Board of Trustees of the University of Arkansas concerning MHD technologies and methods. The other authors declare no competing financial interest.

■ ACKNOWLEDGMENTS

This work was supported by the "Center for Solvation Science ZEMOS" funded by the German Federal Ministry of Education and Research BMBF and by the Ministry of Culture and Research of Nord Rhine-Westphalia. We give special thanks to Dr. Yen-Ting Chen, in the Center for Solvation Science ZEMOS, Ruhr Universität Bochum, for use of the plasma cleaner. We are grateful to Mathew D. Gerner for the initial chip design and the use of the High-Density Electronics Center for chip fabrication.

■ ABBREVIATIONS

DFM	dark-field microscopy
RMHD	redox magnetohydrodynamics
NP	nanoparticle
TEM	transmission electron microscopy
SEM	scanning electron microscopy
DLS	dynamic light scattering
NTA	nanoparticle tracking analysis
LSPR	localized surface plasmon resonance
RMHD−DFM	redox magnetohydrodynamics with dark-field microscopy
PEDOT	poly(3,4-ethylenedioxythiophene)
Ag	silver
SiO_2@Au	silica core gold shell
WE	working electrode
CV	cyclic voltammetry
CE	counter electrode
RE	reference electrode
CP	chronopotentiometry
STEM	scanning transmission electron microscopy
EDX	energy-dispersive X-ray
MSD	mean-square displacement

■ REFERENCES

(1) Hervés, P.; Pérez-Lorenzo, M.; Liz-Marzán, L. M.; Dzubiella, J.; Lu, Y.; Ballauff, M. Catalysis by metallic nanoparticles in aqueous solution: model reactions. *Chem. Soc. Rev.* **2012**, *41*, 5577.

(2) Ananikov, V. P.; Beletskaya, I. P. Toward the Ideal Catalyst: From Atomic Centers to a "Cocktail" of Catalysts. *Organometallics* **2012**, *31*, 1595−1604.

(3) Wildgoose, G. G.; Banks, C. E.; Compton, R. G. Metal Nanoparticles and Related Materials Supported on Carbon Nanotubes: Methods and Applications. *Small* **2006**, *2*, 182−193.

(4) Banin, U.; Waiskopf, N.; Hammarström, L.; Boschloo, G.; Freitag, M.; Johansson, E. M. J.; Sá, J.; Tian, H.; Johnston, M. B.; Herz, L. M.; Milot, R. L.; Kanatzidis, M. G.; Ke, W.; Spanopoulos, I.; Kohlstedt, K. L.; Schatz, G. C.; Lewis, N.; Meyer, T.; Nozik, A. J.; Beard, M. C.; Armstrong, F.; Megarity, C. F.; Schmuttenmaer, C. A.; Batista, V. S.; Brudvig, G. W. Nanotechnology for catalysis and solar energy conversion. *Nanotechnology* **2021**, *32*, 042003.

(5) Linic, S.; Aslam, U.; Boerigter, C.; Morabito, M. Photochemical transformations on plasmonic metal nanoparticles. *Nat. Mater.* **2015**, *14*, 567−576.

(6) Dakal, T. C.; Kumar, A.; Majumdar, R. S.; Yadav, V. Mechanistic Basis of Antimicrobial Actions of Silver Nanoparticles. *Front. Microbiol.* **2016**, *7*, 1831.

(7) El Arrassi, A.; Bellova, P.; Javid, S. M.; Motemani, Y.; Khare, C.; Sengstock, C.; Köller, M.; Ludwig, A.; Tschulik, K. A Unified Interdisciplinary Approach to Design Antibacterial Coatings for Fast Silver Release. *ChemElectroChem* **2017**, *4*, 1975−1983.

(8) Robbins, E. J.; Leckenby, R. E.; Willis, P. The ionization potentials of clustered sodium atoms. *Adv. Phys.: X* **1967**, *16*, 739−744.

(9) Liang, T.; Zhou, D.; Wu, Z.; Shi, P. Size-dependent melting modes and behaviors of Ag nanoparticles: a molecular dynamics study. *Nanotechnology* **2017**, *28*, 485704.

(10) de Heer, W. A. The physics of simple metal clusters: experimental aspects and simple models. *Rev. Mod. Phys.* **1993**, *65*, 611−676.

(11) Chao, Y.-J.; Lyu, Y.-P.; Wu, Z.-W.; Lee, C.-L. Seed-mediated growth of Ag nanocubes and their size-dependent activities toward oxygen reduction reaction. *Int. J. Hydrogen Energy* **2016**, *41*, 3896−3903.

(12) Narayanan, R.; El-Sayed, M. A. Shape-Dependent Catalytic Activity of Platinum Nanoparticles in Colloidal Solution. *Nano Lett.* **2004**, *4*, 1343−1348.

(13) Liz-Marzán, L. M. Tailoring Surface Plasmons through the Morphology and Assembly of Metal Nanoparticles. *Langmuir* **2006**, *22*, 32−41.

(14) Linnemann, J.; Kanokkanchana, K.; Tschulik, K. Design Strategies for Electrocatalysts from an Electrochemist's Perspective. *ACS Catal.* **2021**, *11*, 5318−5346.

(15) Chernousova, S.; Epple, M. Silver as antibacterial agent: ion, nanoparticle, and metal. *Angew. Chem., Int. Ed.* **2013**, *52*, 1636−1653.

(16) Xu, L.; Liang, H.-W.; Yang, Y.; Yu, S.-H. Stability and Reactivity: Positive and Negative Aspects for Nanoparticle Processing. *Chem. Rev.* **2018**, *118*, 3209−3250.

(17) Li, X.; Lenhart, J. J.; Walker, H. W. Aggregation Kinetics and Dissolution of Coated Silver Nanoparticles. *Langmuir* **2012**, *28*, 1095−1104.

(18) Valdiglesias, V.; Costa, C.; Kiliç, G.; Costa, S.; Pásaro, E.; Laffon, B.; Teixeira, J. P. Neuronal cytotoxicity and genotoxicity induced by zinc oxide nanoparticles. *Environ. Int.* **2013**, *55*, 92−100.

(19) Gorka, D. E.; Osterberg, J. S.; Gwin, C. A.; Colman, B. P.; Meyer, J. N.; Bernhardt, E. S.; Gunsch, C. K.; DiGulio, R. T.; Liu, J. Reducing Environmental Toxicity of Silver Nanoparticles through Shape Control. *Environ. Sci. Technol.* **2015**, *49*, 10093−10098.

(20) Loza, K.; Diendorf, J.; Sengstock, C.; Ruiz-Gonzalez, L.; Gonzalez-Calbet, J. M.; Vallet-Regi, M.; Köller, M.; Epple, M. The dissolution and biological effects of silver nanoparticles in biological media. *J. Mater. Chem. B* **2014**, *2*, 1634.

(21) Pu, S.; Gong, C.; Robertson, A. W. Liquid cell transmission electron microscopy and its applications. *R. Soc. Open Sci.* **2020**, *7*, 191204.

(22) Ramos, A. P. Dynamic Light Scattering Applied to Nanoparticle Characterization. In *Nanocharacterization Techniques*; Róz, A. L. D., Leite, F. d. L., Ferreira, M., Oliveira, O. N., Eds.; William Andrew, 2017; pp 99−110.

(23) Malvern Panalytical. Nanopartikel-Tracking-Analyse (NTA). https://www.malvernpanalytical.com/de/products/technology/light-scattering/nanoparticle-tracking-analysis (accessed Oct 01, 2021).

(24) Stramski, D.; Tatarkiewicz, J.; Reynolds, R.; Karr, M. *Nanoparticle analyzer. 14/730,138*; Malvern Panalytical, 1985.

(25) ViewSizer 3000, Horiba. https://www.horiba.com/en_en/products/detail/action/show/Product/viewsizer-3000-1862/(accessed Nov 24, 2021).

(26) Garcia, A.; Wang, S.; Tao, N.; Shan, X.; Wang, Y. Plasmonic Imaging of Oxidation and Reduction of Single Gold Nanoparticles and Their Surface Structural Dynamics. *ACS Sens.* **2021**, *6*, 502−507.

(27) Qiu, K.; Fato, T. P.; Wang, P.-Y.; Long, Y.-T. Real-time monitoring of electrochemical reactions on single nanoparticles by

https://doi.org/10.1021/acsphyschemau.1c00046
ACS Phys. Chem Au 2022, 2, 289−298

dark-field and Raman microscopy. *Dalton Trans.* **2019**, *48*, 3809−3814.
(28) Yang, M.; Batchelor-McAuley, C.; Barton, S.; Rickaby, R. E. M.; Bouman, H. A.; Compton, R. G. Opto-Electrochemical Dissolution Reveals Coccolith Calcium Carbonate Content. *Angew. Chem., Int. Ed.* **2021**, *60*, 20999−21006.
(29) Lemineur, J.-F.; Ciocci, P.; Noël, J.-M.; Ge, H.; Combellas, C.; Kanoufi, F. Imaging and Quantifying the Formation of Single Nanobubbles at Single Platinum Nanoparticles during the Hydrogen Evolution Reaction. *ACS Nano* **2021**, *15*, 2643−2653.
(30) Willets, K. A.; van Duyne, R. P. Localized surface plasmon resonance spectroscopy and sensing. *Annu. Rev. Phys. Chem.* **2007**, *58*, 267−297.
(31) Willets, K. A.; Wilson, A. J.; Sundaresan, V.; Joshi, P. B. Super-Resolution Imaging and Plasmonics. *Chem. Rev.* **2017**, *117*, 7538−7582.
(32) Faraday, M. LIX. Experimental relations of gold (and other metals) to light.-The bakerian lecture. *Philos. Mag.* **1857**, *14*, 512−539.
(33) Wagner, T.; Lipinski, H.-G.; Wiemann, M. Dark field nanoparticle tracking analysis for size characterization of plasmonic and non-plasmonic particles. *J. Nanopart. Res.* **2014**, *16*, 2419.
(34) Huang, X.; El-Sayed, I. H.; Qian, W.; El-Sayed, M. A. Cancer Cell Imaging and Photothermal Therapy in the Near-Infrared Region by Using Gold Nanorods. *J. Am. Chem. Soc.* **2006**, *128*, 2115−2120.
(35) McFarland, A. D.; van Duyne, R. P. Single Silver Nanoparticles as Real-Time Optical Sensors with Zeptomole Sensitivity. *Nano Lett.* **2003**, *3*, 1057−1062.
(36) Sherry, L. J.; Chang, S.-H.; Schatz, G. C.; van Duyne, R. P.; Wiley, B. J.; Xia, Y. Localized Surface Plasmon Resonance Spectroscopy of Single Silver Nanocubes. *Nano Lett.* **2005**, *5*, 2034−2038.
(37) Wonner, K.; Evers, M. V.; Tschulik, K. Simultaneous Opto- and Spectro-Electrochemistry: Reactions of Individual Nanoparticles Uncovered by Dark-Field Microscopy. *J. Am. Chem. Soc.* **2018**, *140*, 12658−12661.
(38) Wang, H.; Zhang, T.; Zhou, X. Dark-field spectroscopy: development, applications and perspectives in single nanoparticle catalysis. *J. Phys.: Condens. Matter* **2019**, *31*, 473001.
(39) Wang, K.; Shangguan, L.; Liu, Y.; Jiang, L.; Zhang, F.; Wei, Y.; Zhang, Y.; Qi, Z.; Wang, K.; Liu, S. In Situ Detection and Imaging of Telomerase Activity in Cancer Cell Lines via Disassembly of Plasmonic Core-Satellites Nanostructured Probe. *Anal. Chem.* **2017**, *89*, 7262−7268.
(40) Wonner, K.; Rurainsky, C.; Tschulik, K. Operando Studies of the Electrochemical Dissolution of Silver Nanoparticles in Nitrate Solutions Observed With Hyperspectral Dark-Field Microscopy. *Front. Chem.* **2020**, *7*, 912.
(41) Wonner, K.; Murke, S.; Alfarano, S. R.; Hosseini, P.; Havenith, M.; Tschulik, K. Operando electrochemical SERS monitors nanoparticle reactions by capping agent fingerprints. *Nano Res.* **2022**, DOI: 10.1007/s12274-021-3999-2.
(42) Matsuura, Y.; Ouchi, N.; Nakamura, A.; Kato, H. Determination of an accurate size distribution of nanoparticles using particle tracking analysis corrected for the adverse effect of random Brownian motion. *Phys. Chem. Chem. Phys.* **2018**, *20*, 17839−17846.
(43) Ma, W.; Ma, H.; Chen, J.-F.; Peng, Y.-Y.; Yang, Z.-Y.; Wang, H.-F.; Ying, Y.-L.; Tian, H.; Long, Y.-T. Tracking motion trajectories of individual nanoparticles using time-resolved current traces. *Chem. Sci.* **2017**, *8*, 1854−1861.
(44) Lee, B. H.; Park, H. Y. HybTrack: A hybrid single particle tracking software using manual and automatic detection of dim signals. *Sci. Rep.* **2018**, *8*, 212.
(45) Zhang, F.; Durham, P.; Sayes, C. M.; Lau, B. L. T.; Bruce, E. D. Particle uptake efficiency is significantly affected by type of capping agent and cell line. *J. Appl. Toxicol.* **2015**, *35*, 1114−1121.
(46) Zeng, W.; Jacobi, I.; Beck, D. J.; Li, S.; Stone, H. A. Characterization of syringe-pump-driven induced pressure fluctuations in elastic microchannels. *Lab Chip* **2015**, *15*, 1110−1115.
(47) Ghosal, S. Fluid mechanics of electroosmotic flow and its effect on band broadening in capillary electrophoresis. *Electrophoresis* **2004**, *25*, 214−228.
(48) Nash, C. K.; Fritsch, I. Poly(3,4-ethylenedioxythiophene)-Modified Electrodes for Microfluidics Pumping with Redox-Magnetohydrodynamics: Improving Compatibility for Broader Applications by Eliminating Addition of Redox Species to Solution. *Anal. Chem.* **2016**, *88*, 1601−1609.
(49) Fritsch, I.; Carter, C. S.; Aguilar, Z. P. Microfluidics and Small Volume Mixing Based on Redox Magnetohydrodynamics Methods. U.S. Patent 20,030,118,453 A1.
(50) Khan, F. Z.; Hutcheson, J. A.; Hunter, C. J.; Powless, A. J.; Benson, D.; Fritsch, I.; Muldoon, T. J. Redox-Magnetohydrodynamically Controlled Fluid Flow with Poly(3,4-ethylenedioxythiophene) Coupled to an Epitaxial Light Sheet Confocal Microscope for Image Cytometry Applications. *Anal. Chem.* **2018**, *90*, 7862−7870.
(51) Leventis, N.; Gao, X. Magnetohydrodynamic Electrochemistry in the Field of Nd−Fe−B Magnets. Theory, Experiment, and Application in Self-Powered Flow Delivery Systems. *Anal. Chem.* **2001**, *73*, 3981−3992.
(52) Leventis, N.; Gao, X. Nd−Fe−B Permanent Magnet Electrodes. Theoretical Evaluation and Experimental Demonstration of the Paramagnetic Body Forces. *J. Am. Chem. Soc.* **2002**, *124*, 1079−1088.
(53) Khan, F. Z.; Fritsch, I. Chip-Scale Electrodeposition and Analysis of Poly(3,4-ethylenedioxythiophene) (PEDOT) Films for Enhanced and Sustained Microfluidics Using DC-Redox-Magnetohydrodynamics. *J. Electrochem. Soc.* **2019**, *166*, H615−H627.
(54) Gao, F.; Kreidermacher, A.; Fritsch, I.; Heyes, C. D. 3D Imaging of Flow Patterns in an Internally-Pumped Microfluidic Device: Redox Magnetohydrodynamics and Electrochemically-Generated Density Gradients. *Anal. Chem.* **2013**, *85*, 4414−4422.
(55) Noël, J.-M.; Lemineur, J.-F. Optical microscopy to study single nanoparticles electrochemistry: From reaction to motion. *Curr. Opin. Electrochem.* **2021**, *25*, 100647.
(56) Wang, R.; Ji, X.; Huang, Z.; Xue, Y.; Wang, D.; Yang, W. Citrate-Regulated Surface Morphology of SiO2@Au Particles To Control the Surface Plasmonic Properties. *J. Phys. Chem. C* **2016**, *120*, 377−385.
(57) Nehl, C. L.; Grady, N. K.; Goodrich, G. P.; Tam, F.; Halas, N. J.; Hafner, J. H. Scattering Spectra of Single Gold Nanoshells. *Nano Lett.* **2004**, *4*, 2355−2359.
(58) Sahore, V.; Fritsch, I. Flat Flow Profiles Achieved with Microfluidics Generated by Redox-Magnetohydrodynamics. *Anal. Chem.* **2013**, *85*, 11809−11816.
(59) Schindelin, J.; Arganda-Carreras, I.; Frise, E.; Kaynig, V.; Longair, M.; Pietzsch, T.; Preibisch, S.; Rueden, C.; Saalfeld, S.; Schmid, B.; Tinevez, J.-Y.; White, D. J.; Hartenstein, V.; Eliceiri, K.; Tomancak, P.; Cardona, A. Fiji: an open-source platform for biological-image analysis. *Nat. Methods* **2012**, *9*, 676−682.
(60) Sbalzarini, I. F.; Koumoutsakos, P. Feature point tracking and trajectory analysis for video imaging in cell biology. *J. Struct. Biol.* **2005**, *151*, 182−195.
(61) Tinevez, J.-Y.; Perry, N.; Schindelin, J.; Hoopes, G. M.; Reynolds, G. D.; Laplantine, E.; Bednarek, S. Y.; Shorte, S. L.; Eliceiri, K. W. TrackMate: An open and extensible platform for single-particle tracking. *Methods* **2017**, *115*, 80−90.
(62) Ernst, D.; Köhler, J. How the number of fitting points for the slope of the mean-square displacement influences the experimentally determined particle size distribution from single-particle tracking. *Phys. Chem. Chem. Phys.* **2013**, *15*, 3429.
(63) Ando, J.; Nakamura, A.; Yamamoto, M.; Song, C.; Murata, K.; Iino, R. Multicolor High-Speed Tracking of Single Biomolecules with Silver, Gold, and Silver-Gold Alloy Nanoparticles. *ACS Photonics* **2019**, *6*, 2870−2883.
(64) Finder, C.; Wohlgemuth, M.; Mayer, C. Analysis of Particle Size Distribution by Particle Tracking. *Part. Part. Syst. Charact.* **2004**, *21*, 372−378.

(65) Nenasheva, T. A.; Carter, T.; Mashanov, G. I. Automatic tracking of individual migrating cells using low-magnification dark-field microscopy. *J. Microsc.* **2012**, *246*, 83−88.
(66) Verpillat, F.; Joud, F.; Desbiolles, P.; Gross, M. Dark-field digital holographic microscopy for 3D-tracking of gold nanoparticles. *Opt. Express* **2011**, *19*, 26044−26055.
(67) Ma, Y.; Wang, X.; Liu, H.; Wei, L.; Xiao, L. Recent advances in optical microscopic methods for single-particle tracking in biological samples. *Anal. Bioanal. Chem.* **2019**, *411*, 4445−4463.
(68) Miller, C. C. The Stokes-Einstein law for diffusion in solution. *Proc. R. Soc. London, Ser. A* **1924**, *106*, 724−749.
(69) Walker, J. G. Improved nano-particle tracking analysis. *Meas. Sci. Technol.* **2012**, *23*, 065605.
(70) Haehnel, V.; Khan, F. Z.; Mutschke, G.; Cierpka, C.; Uhlemann, M.; Fritsch, I. Combining magnetic forces for contactless manipulation of fluids in microelectrode-microfluidic systems. *Sci. Rep.* **2019**, *9*, 5103.
(71) Sahore, V.; Fritsch, I. Redox-Magnetohydrodynamics, Flat Flow Profile-Guided Enzyme Assay Detection: Toward Multiple, Parallel Analyses. *Anal. Chem.* **2014**, *86*, 9405−9411.
(72) Ngamchuea, K.; Tschulik, K.; Compton, R. G. Magnetic control: Switchable ultrahigh magnetic gradients at Fe3O4 nanoparticles to enhance solution-phase mass transport. *Nano Res.* **2015**, *8*, 3293−3306.
(73) Yang, X.; Tschulik, K.; Uhlemann, M.; Odenbach, S.; Eckert, K. Enrichment of Paramagnetic Ions from Homogeneous Solutions in Inhomogeneous Magnetic Fields. *J. Phys. Chem. Lett.* **2012**, *3*, 3559−3564.
(74) Tschulik, K.; Cierpka, C.; Mutschke, G.; Gebert, A.; Schultz, L.; Uhlemann, M. Clarifying the Mechanism of Reverse Structuring during Electrodeposition in Magnetic Gradient Fields. *Anal. Chem.* **2012**, *84*, 2328−2334.
(75) Tschulik, K.; Compton, R. G. Nanoparticle impacts reveal magnetic field induced agglomeration and reduced dissolution rates. *Phys. Chem. Chem. Phys.* **2014**, *16*, 13909−13913.

https://doi.org/10.1021/acsphyschemau.1c00046
ACS Phys. Chem Au 2022, 2, 289−298